Additive Manufacturing 40 (2021) 101915

Contents lists available at ScienceDirect

Additive Manufacturing

journal homepage: www.elsevier.com/locate/addma

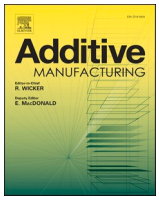

Research Paper

Detection and location of microdefects during selective laser melting by wireless acoustic emission measurement

Kaita Ito [a,*], Masahiro Kusano [b], Masahiko Demura [a], Makoto Watanabe [b]

[a] National Institute for Materials Science, 1-1 Namiki, Tsukuba, Ibaraki 305-0044, Japan
[b] National Institute for Materials Science, 1-2-1 Sengen, Tsukuba, Ibaraki 305-0047, Japan

ARTICLE INFO

Keywords:
Selective laser melting
Crack detection
Acoustic emission
Wireless monitoring
Real-time monitoring

ABSTRACT

Microdefects sometimes form in workpieces fabricated by selective laser melting (SLM). It is difficult to understand the mechanism of generation of microdefects because the occurrence time during processing cannot be easily identified by conventional monitoring methods. We have therefore developed a convenient method for real-time monitoring of microdefects generation during SLM by using proprietary battery-powered equipment capable of continuous recording and wireless transmission of acoustic emission (AE) waveforms. To clarify the detection capabilities of the proposed method and to evaluate the factors that cause microcrack generation, AE monitoring was conducted for single-layer modeling tests with single-track or multi-track. We could successfully detect AE signals during the tests. The times of occurrence and locations of AE events were identified, and the results were compared with observations of the specimen cross-sections by the X-ray computed tomography (CT). At first in single-track tests, burst type AE events were detected during processing and their origin was confirmed to be pores and microcracks in the specimen. Then in multi-track tests, defects slightly after laser irradiation and defects due to the turning back of the irradiation were detected. The effectiveness and potential of our novel AE monitoring technique for the SLM process have been demonstrated.

1. Introduction

Additive manufacturing methods have recently attracted considerable attention because they permit the manufacture of items with three-dimensional complex shapes by direct forming from raw material likes powders or wires, without any machining. Selective laser melting (SLM) is a powder bed fusion 3D additive manufacturing process that uses a laser as the heat source and intense research and development efforts are ongoing [1]. Especially in the aerospace engineering sector, this method represents a new manufacturing process for high-strength difficult-to--machining materials such as nickel alloys. However, the generation of microdefects during SLM processing is a major problem in manufacturing of parts made from nickel alloys such as Hastelloy X, which has excellent high-temperature mechanical properties. Therefore, studies on cracking behavior and attempts to suppress microcrack generation by composition control or by addition of carbides have been conducted [1,2]. In general, SLM processes are conducted in an inert atmosphere, where a powder bed is prepared on a stage, and melting and solidification processes are repeatedly performed by using a fast laser scan. Consequently, elucidation of the cracking mechanism is difficult because it is not possible to easily determine when the microdefects form in the workpiece. As a consequence, crack monitoring techniques are required during SLM processing.

Acoustic emission (AE) method is a non-destructive evaluation technique that might be able to handle this task. AE analysis has a wide variety of applications, ranging from mechanical testing of small specimens to the structural health monitoring of huge infrastructure and industrial facilities. Moreover, AE method has recently been applied in monitoring the manufacturing process of materials. The method permits the detection of rapid deformation events in a material *e.g.* fractures or friction by using acoustic waves with a frequency from a few tens to several hundreds of kilohertz emitted during the event. Therefore, AE method can detect occurrences of events in real-time, unlike typical non-destructive flaw detection methods that uses X-rays or ultrasound.

In an application of AE monitoring to SLM processing, Shevchik et al. [3–5] made an *in-situ* quality monitoring under different modeling conditions. Using a neural network, they showed that the quality of the processed material can be estimated from the time-frequency characteristics (wavelet transform results) of the AE waveforms. They also captured the process of microdefect formation during modeling by

* Corresponding author.
E-mail address: ITO.Kaita@nims.go.jp (K. Ito).

https://doi.org/10.1016/j.addma.2021.101915
Received 4 September 2020; Received in revised form 8 February 2021; Accepted 14 February 2021
Available online 17 February 2021

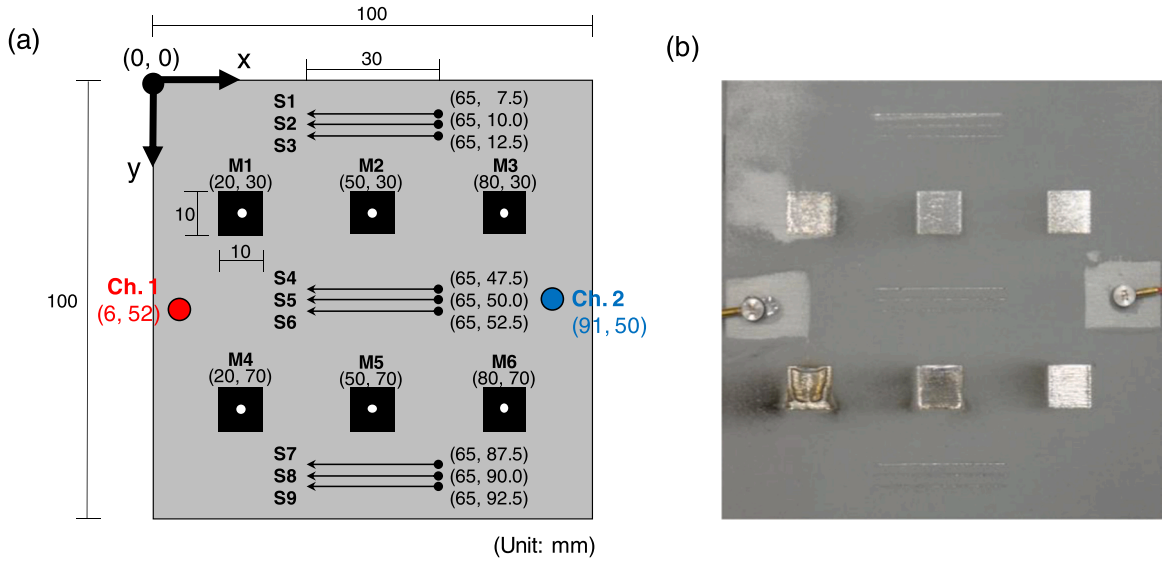

Fig. 1. (a) Position of processed items on the substrate and (b) Photograph of the substrate after processing.

high-speed X-ray observation and compared the wavelet transform results of AE waveforms, and showed the difference in the frequency components of AE during the microdefect formation. Eschner et al. [6] used a common piezoelectric sensor to estimate the density of the processed material from the time-frequency characteristics of the AE waveform. These monitoring and analysis methods are very effective, but it is just a rough evaluation and does not include precise information from AE events such as the source location. On the other hand, attaching multiple piezoelectric sensors on the specimen surface permits the detection of the AE source location from the differences between the arrival times of AE wave at each sensor; this is the same method that is used to locate the epicenter of an earthquake. The source location of a particular AE event would be as valuable information as the occurrence time in process monitoring. For example, during the laser cladding process, which is similar to the SLM method in the sense that it uses a laser for material processing, Wang et al. [7] used two sensors to correspond AE events and cracks along the processing line. However, the SLM process is conducted in an airtight chamber, so that connecting the many power and communication wires for AE measurement by using airtight connectors is not straightforward. Consequently, a non-contact AE measurement method is desirable. Kouprianoff et al. [8]. attempted to detect the AE during SLM processing with a microphone by capturing the vibration propagating from inside the material into the air. Prieto et al. [9] developed a unique optical microphone to detect AE during laser cladding process and made a precise evaluation. However, using air-coupled sensors such as microphones, AE source localization by multiple sensors is difficult. Therefore, another non-contact AE measurement method is laser AE, which uses laser interferometers as sensors [10,11]. The authors of this paper have previously worked on this option; Watanabe et al. [12,13] developed a laser AE measurement method that uses heterodyne interferometers, whereas Ito et al. [14,15] succeeded in applying this method to detect cracks during processes in difficult-to-measure environments such as thermal spraying for deposition of ceramic coating. However, there are drawbacks. Laser interferometers are less sensitive than piezoelectric sensors, and precise optical path controlling is required.

Another option for more convenient wireless measurement would be to use a system in which generic piezoelectric sensors and small battery-powered measuring equipment with wireless transmission function [16]. Such wireless measurement system would eliminate most of cabling efforts. However, the computing capacity of such a battery-powered system is limited by the need to minimize power consumption, and consequently only limited amounts of data set without its waveform can be obtained for each AE event. Digital filtering to remove noise from laser irradiation and from mechanical action during processing, as well the acquisition of the massive amounts of waveform data necessary to analyze the mechanism underlying the AE are unavailable in such systems.

Therefore, conventional piezoelectric sensors and an original battery-powered proprietary measurement equipment are used in this study. The measurement equipment can transmit entire AE waveforms, as they are continuously measured, by using high-speed Wi-Fi. This eliminates the limitations on data processing that are inherent in the use of a battery-powered computer. Instead, a high-performance computer outside the processing equipment receives and analyzes the continuous waveforms. Moreover, if better waveform-analysis procedures were to be discovered after an experiment, further analysis would be possible by replaying the continuous waveforms stored at the receiving end, eliminating the need for additional experiments.

In this study, our aim was to demonstrate that the occurrence time and location for microdefects in a SLM process can be detected by using this newly developed wireless AE process-monitoring equipment. To confirm the accuracy of the detected time and location at first, processing was conducted in a single-layer tests instead of multi-layer test. The correlation among the laser-irradiation position, the source location of AE events, and the positions of microdefects found in sample observation after SLM processing was investigated.

2. Experiments

The processing of a single layer by SLM was monitored by AE method. Two kinds of tests were conducted: a single-track test in which only one line was irradiated and a multi-track test in which a square region was irradiated in a zigzag pattern that covered the plane.

2.1. Processing conditions

SLM 280 HL equipment from SLM Solutions Group AG (Lübeck) was used for processing. The laser wavelength was 1064 nm. The substrate consisted of Hastelloy X and had dimensions of 100 × 100 × 2.0 mm. Hastelloy X powder (AMPERPRINT 0228; Höganäs AB, Höganäs), a Ni alloy containing Cr (22.1 mass%), Fe (18.1 mass%), and Mo (9.0 mass %), with a particle size of 15–45 μm was levelled to a thickness of 50 μm on the substrate. The irradiating laser was focused to a spot with a diameter of 80 μm (Gaussian curve).

Single-track tests were conducted by irradiating a 30-mm-long line at

Table 1
Single-track test conditions.

Test ID	Laser power (W)	Scanning speed (mm s^{-1})
S1, S4, S7	700	250
S2, S5, S8	700	900
S3, S6, S9	300	900

Table 2
Multi-track test conditions.

Test ID	Laser power (W)	Hatch distance (μm)
M1	540	100
M2	360	100
M3	180	100
M4	540	25
M5	360	25
M6	180	25

various laser powers and scanning speeds. Three tests were conducted for each set of conditions at different places on the substrate. In multi-track tests, the laser power and hatch distance were changed while the scanning speed was fixed at 900 mm/s, and the irradiation covered a region measuring 10 × 10 mm. Only one test was conducted for each set of conditions. However, since a multi-track test includes 100 or 400 tracks, the effects of adjacent tracks and the effects of zig-zag scanning can be evaluated repeatedly enough times in a single test. Fig. 1 shows the processing positions and a photograph of the substrate after processing. Tables 1 and 2 list the conditions for the single-track and multi-track tests, respectively. Conditions M3 in the multi-track tests, which had the lowest input energy density, corresponded to those used in practice. Other conditions had higher input energies were tried to induce cracks intentionally. Tests were conducted in the order S1, S2, …, S9, M1, M2, …, and M6, and the interval between successive tests was more than two minutes.

2.2. AE measurement conditions

Piezoelectric AE sensors (AE254-SMH0177-0019; Fuji Ceramics Corp., Shizuoka) were used. These sensors are small, with a diameter of 5 mm and a height of 4 mm. Their resonance frequency is 250 kHz, and it shows relatively flat and high sensitivity between 150 and 600 kHz, except around the resonant frequency. Also, this sensor has a higher heat resistance than other general PZT sensors, with a heat resistance temperature of 450 K. The sensors were attached to a clean substrate, without any powder, by using a cyanoacrylate adhesive (Aron Alpha, Toagosei Co. Ltd., Tokyo). The heat resistant temperature of the adhesive is about 350 K, which is below the heat resistant temperature of the AE sensors. Therefore, if the temperature of the substrate becomes too high during processing, the sensors are protected consequently because the adhesive peels off before the sensor reaches the heat resistant temperature. However, the sensor did not delaminate in this test and it was determined that the temperature was not excessively high. The sensors ch. 1 and ch. 2 were to be attached at symmetrical positions with respect to the center of the substrate, *i.e.*, $(x, y) = (10\text{ mm}, 50\text{ mm})$ and (90 mm, 50 mm), respectively. However, there were installation errors of a few millimeters. As shown in Fig. 1, ch. 1 and ch. 2 were actually attached at (6 mm, 52 mm) and (91 mm, 50 mm), respectively. In this study, the evaluation point of the waveform is to find the rising point *i.e.* arrival time of the AE wave to the sensor. Also, the influence of the heat of the specimen on the sensor must be avoided as much as possible, especially in multi-track experiments. Therefore, it is important to note that the waveform after the arrival time includes multiple reflected components from the edges of the substrate. And other thing to keep in mind, there was a relatively large individual difference in sensitivity between the sensors used in this experiment. According to the calibration certificates of both sensors, in the frequency band around the resonance frequency, the sensitivity of ch. 2 was about 5–10 dB higher than that of ch. 1. Then, in the waveforms shown below, ch. 2 may have an amplitude that is three times larger than that of ch. 1. However, the arrival time of the AE wave can be detected without any problem even in ch. 1. This difference in sensitivity was acceptable since the purpose of this study can be achieved if the arrival time of the AE wave can be detected by each sensor. However, when conducting experiments where it is important to compare the amplitudes of AE events detected by different sensors, a set of sensors with similar sensitivity should be selected based on the calibration certificate of the sensor or the detected amplitude of artificial AEs that have been measured under constant conditions.

The AE sensors were connected to a wireless sensor node, developed by Ito, one of the authors of this paper, by using 0.5 m-long low-noise coaxial cables [17]. The sensor node uses a RedPitaya STEMLab 125-14 board (https://www.redpitaya.com/), and high-quality continuous sampling was made possible by using nonstandard firmware. The output voltages of the two AE sensors were continuously sampled at a sampling frequency of 1.95 MHz (1/64th of 125 MHz) with a resolution of 14 bits. AE measurements were continued without interruption from about 30 s before starting the first test (S1) to few tens of minutes after the end of the last test (M6). The raw (as-measured) waveform data were transmitted to analysis equipment located outside the SLM processing equipment by using high speed Wi-Fi (IEEE 802.11ac standard; theoretical maximum speed: 433 Mbps). The analysis equipment employed a continuous wave memory (CWM) system, also developed by Ito, that is capable of performing continuous AE waveform measurements and analyses [14,15,18].

The power consumption of the wireless sensor node was about 4 W, and power was supplied from a commercially available mobile Li-ion battery for smartphones. No wired connections to the outside of the SLM processing equipment were therefore necessary. The maximum capacity of the commercially available mobile Li-ion battery was 100 Wh, permitting the wireless sensor node to be operated continuously for up to about 25 h. This would be a sufficient duration for monitoring of additive manufacturing processes in near future by using current setup. The waveform data were also recorded on a microSDXC card in the sensor node at the same time that they were transferred wirelessly, thereby securing the data in the event of a loss of the Wi-Fi connection for any reason.

In this experiment, the sensors were attached on the same surface as the modeling. This is the simplest installation based on the assumption that only a single-layer monitoring is to be performed. If multi-layer monitoring is to be conducted, the sensor and the wireless node need to be placed on the back surface of the substrate or somewhere to prevent the sensor from contacting with the recoater, However, when the sensors are attached on the backside, there is a slight performance and stability degradation in Wi-Fi data transmission. Furthermore, if a permanent AE measurement system is to be built, there is an option to connect the inside and outside of the chamber with an air-tighten connector to perform wired measurements.

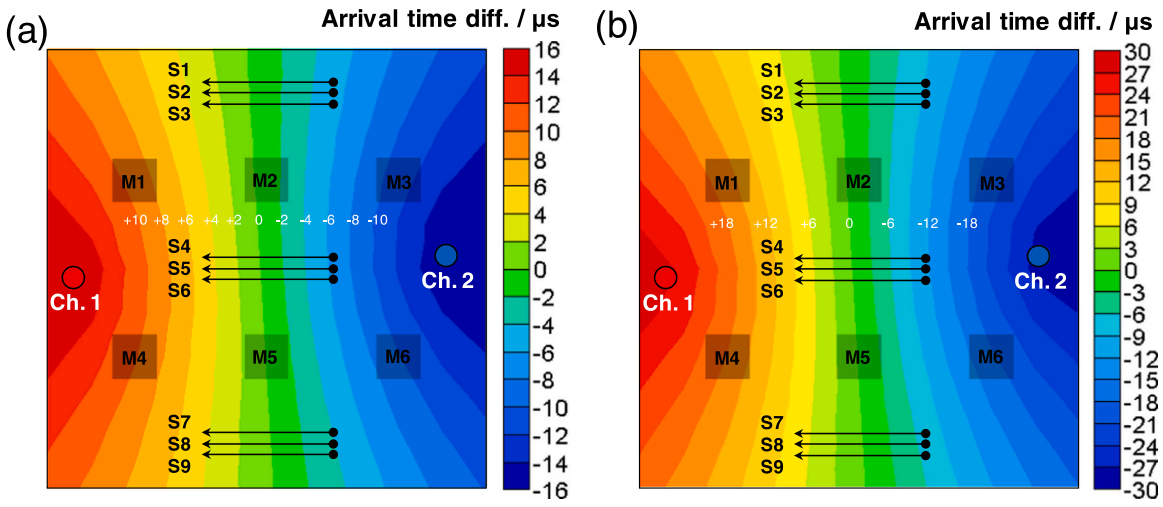

Fig. 2. Difference in time when a (a) the S_0 mode and (b) the A_0 mode Lamb wave reaches ch. 1 and ch. 2 (positive when ch. 1 is earlier).

2.3. AE analysis conditions

The AE continuous waveform obtained by using the waveform-analysis device was processed with a digital noise filter, and burst type AE events were subsequently detected. Source location processing was then conducted for the detected events. These processes are explained below. In addition, the so-called continuous type AE (AE where individual events cannot be separated because many low amplitude events overlap) occurred during laser irradiation. However, since the purpose of this study is to detect local defects such as pores and microcracks, only burst type AE events were evaluated.

The raw AE continuous waveform can contain two typical sources of noise. The first is a component with a frequency of a few tens of kilohertz arising from mechanical vibration of the SLM processing equipment. This noise has a lower frequency than typical AE components, which have a frequency of a few hundred of kilohertz, and it can therefore be removed by using a high pass filter. Preliminary tests in this study confirmed that the vibration noise had frequencies below about 50 kHz; a high pass filter with cutoff frequency of 50 kHz was therefore applied in the main tests. This filter performs spectral subtraction in the frequency domain [19]. Specifically, a short-time Fourier transform, rewriting of intensity values below 50 kHz to zero, and an inverse short-time Fourier transform were applied to the continuous waveforms,

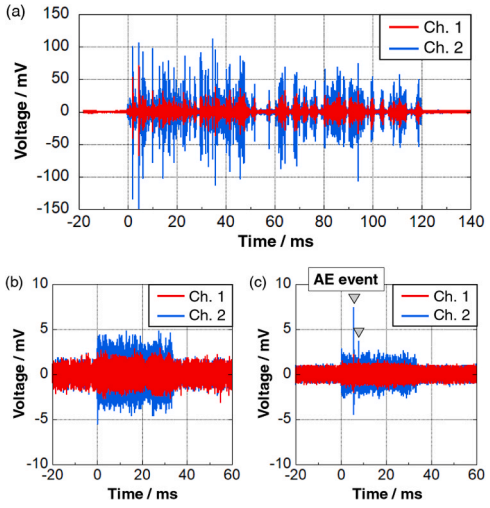

Fig. 3. AE continuous waveform in a single-track test: (a) Test S4 (700 W, 250 mm/s), (b) S5 (700 W, 900 mm/s), and (c) S6 (300 W, 900 mm/s).

in that order. The second source of noise is electrical pulses and continuous noise from laser irradiation and the servo drive of the SLM processing equipment. Electric pulses travel along the following path: processing equipment, specimen, AE sensor, measurement equipment and power line. The pulses act on the analog-to-digital converter, and appear as noise spikes on the waveform data. However, in the present study, the wireless sensor nodes were battery-powered; consequently, there was no electric path through the measurement equipment, and almost no noise spikes were detected. On the other hand, continuous noise acts directly on the piezoelectric element of the sensor and vibrates it at its resonance frequency. This resonance frequency is in the same frequency range as effective AE events and cannot therefore be separated by using a frequency filter. However, the continuous noise detected in the tests was weak. The noise level after eliminating low-frequency noise from mechanical vibration, which is the root-mean-square (RMS) voltage of the continuous waveforms when the laser was not operating, was slightly increased from about 0.4 mV to approximately 0.6 mV. This did not significantly affect event detection.

A general threshold crossing method was used to detect AE events. The threshold voltages for detecting AE events were set to four levels of 2.5, 5, 10, 20 mV, and the union of events detected in each threshold was used [15].

A knowledge of the propagation speed of AE waves is necessary for source location of AE events. There are a number of modes with different sound velocity in AE waves that propagate in a solid material. Two sound velocities of 5.1×10^3 and 2.9×10^3 m/s were detected by generating several artificial AEs of the Hsu-Nielsen source [20], known as "pencil-lead break", at several positions on a straight line connecting the two sensors and measuring the actual sound velocity at several times each. These were assumed to correspond to the S_0 and A_0 modes, respectively, of Lamb waves (a type of surface wave), because the 2 mm thick substrate in the tests is thinner than the wavelength of AE waves (about 12 mm, calculated from the resonance frequency of the sensor of 250 kHz and the sound velocity of 2.9×10^3 m/s), and because the AE source and sensors were on the same plane on the substrate. In general, the S_0 mode is fast, but has a small amplitude, whereas the A_0 mode is slow, but has large amplitude. As a result, the rising edges of both S_0 and A_0 modes would be expected to be detected in large amplitude events, whereas only the rising edge of the A_0 mode should be detectable in small amplitude events, because the S_0 mode is buried in noise. Sound in the air does not affect the AE wave arrival detection because its sound velocity (about 0.35 km/s) is significantly slower than the surface waves. Although the surface wave velocities are likely to be different between the SLM fabricated material and the substrate, the difference may be not significant because the most of the propagation path (a

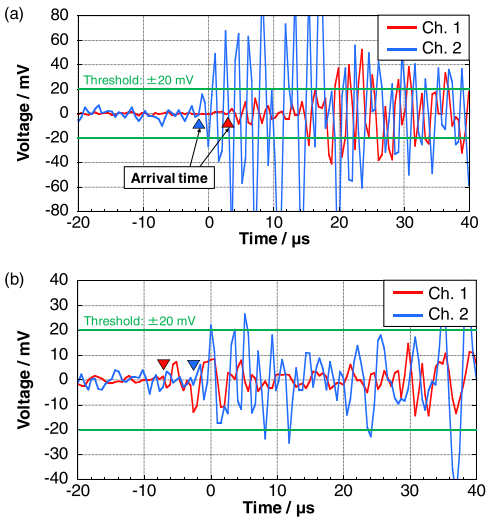

Fig. 4. Burst-type AE event during single-track test S4: (a) 2 ms after starting laser irradiation, and (b) 2 ms before finishing laser irradiation.

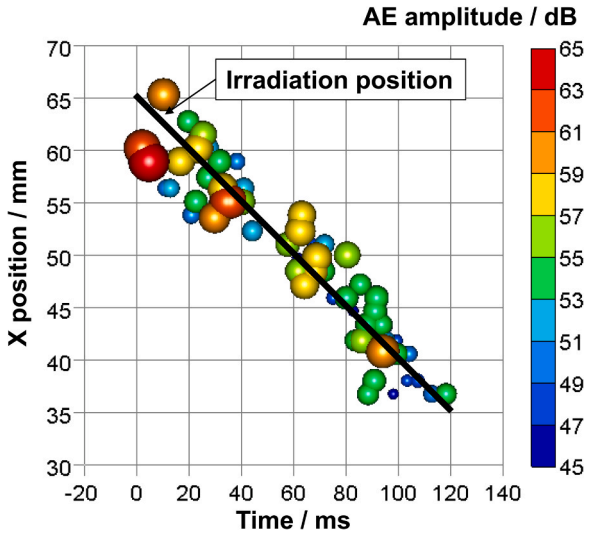

Fig. 5. Relationship between the AE event time, the located position, and the position of laser in the single-track S4 test.

straight line from the AE source to the sensor) is on the substrate even in the multi-track test (See Fig. 1). For these reasons, it is considered that the source location can be simply determined by the surface wave velocities of the substrate.

A two-step Akaike's information criterion (AIC) [21] picker, developed by Sedlak et al. [22], was used to detect waveform arrival times for the purpose of position location. This is already a built-in function of CWM. For each channel, three candidate waveform arrival times were selected by the Sedlak's method, and which of these was the arrival of a wave in the S_0 or A_0 mode was automatically determined from the time differences among 2 ch × 3 candidates by a simple computer program [23]. In most cases, the "candidates" which were not related to the arrival of either the S_0 or A_0 mode were easily eliminated because the times were far away from the trigger time. Fig. 2 shows the estimated time difference in the waveform rising edges between the S_0 and A_0 modes for each position on the specimen. As mentioned above, the sampling frequency f was 1.95 MHz and the speed of sound v was 2.9×10^3 m/s in the slower A_0 mode in the tests; therefore, the resolution for source location was calculated as $v/2f = 0.74$ mm.

3. Results

AE events were detected and their positions were located from the AE continuous waveform after noise removal in both single-track and multi-track tests. The located positions were analyzed together with the laser-irradiation position history. In addition, the specimen after testing was examined by X-ray CT (SMX-160CTS; Shimadzu Corp., Kyoto).

3.1. Single-track tests

Fig. 3 shows examples of AE continuous waveforms after noise reduction obtained in tests S4, S5, and S6. Time 0 ms in the figure is when laser irradiation started. The differences between the three tests under the same conditions were small; therefore, the waveforms of one irradiation each from tests are shown. Tests with the highest energy density at the track (S1, S4, and S7 with 700 W and 250 mm/s) resulted in the detection of a few hundred AE events during laser irradiation. No events were detected before or after laser irradiation. AE source location was only possible in 22% (64 / 289) of the events. It is because a clear rising edge of the waveform could not be identified in small amplitude events or in events immediately after a previous large amplitude event.

Fig. 4 shows the waveform near the rising edge for the first and last AE event where source location was possible in test S4. Time 0 μs in the figure is the trigger time for each event, *i.e.* the time when the waveform amplitude exceeded the threshold for the first time in an event. The waveform arrival time was determined by using the aforementioned two-step AIC picker with the waveform near the trigger time. As a result, the trigger time and waveform arrival time did not match exactly and, generally, the arrival time of the earliest channel was few microseconds earlier than the trigger time. The first detected event in Fig. 4(a) occurred immediately (2 ms) after the start of laser irradiation, and the waveform arrival time was earlier in ch. 2 by 5 μs. On the other hand, the last detected event in Fig. 4(b) was immediately (2 ms) before the end of laser irradiation, and the waveform arrival time was earlier in ch. 1 by 5 μs. Assuming that the AE originated in the track, the event positions are located near the start and near the end of the track, respectively, as shown in Fig. 2. This means that both events happened at almost the same time and location as laser irradiation or, to be more precise, just below the laser spot. Fig. 5 shows the relationship between event time, the source location, and the position of laser irradiation at the event occurrence time for all events where the position could be located in the S4 test. Events occurred near the laser spot, as expected.

Very few AE events were detected when the laser energy density at the track was low. No events were detected in tests S2, S5, or S8 (700 W and 900 mm/s) and few were detected in tests S3, S6, S9 (300 W, 900 mm/s). In test S6, as shown in Fig. 3(c), source location was possible for only one event, which had a relatively large amplitude. Again, the event occurred near the laser spot.

3.2. Multi-track tests

Fig. 6 shows a sample of an AE continuous waveform over 100 ms. Except for the M3 test, where the input energy density was lowest

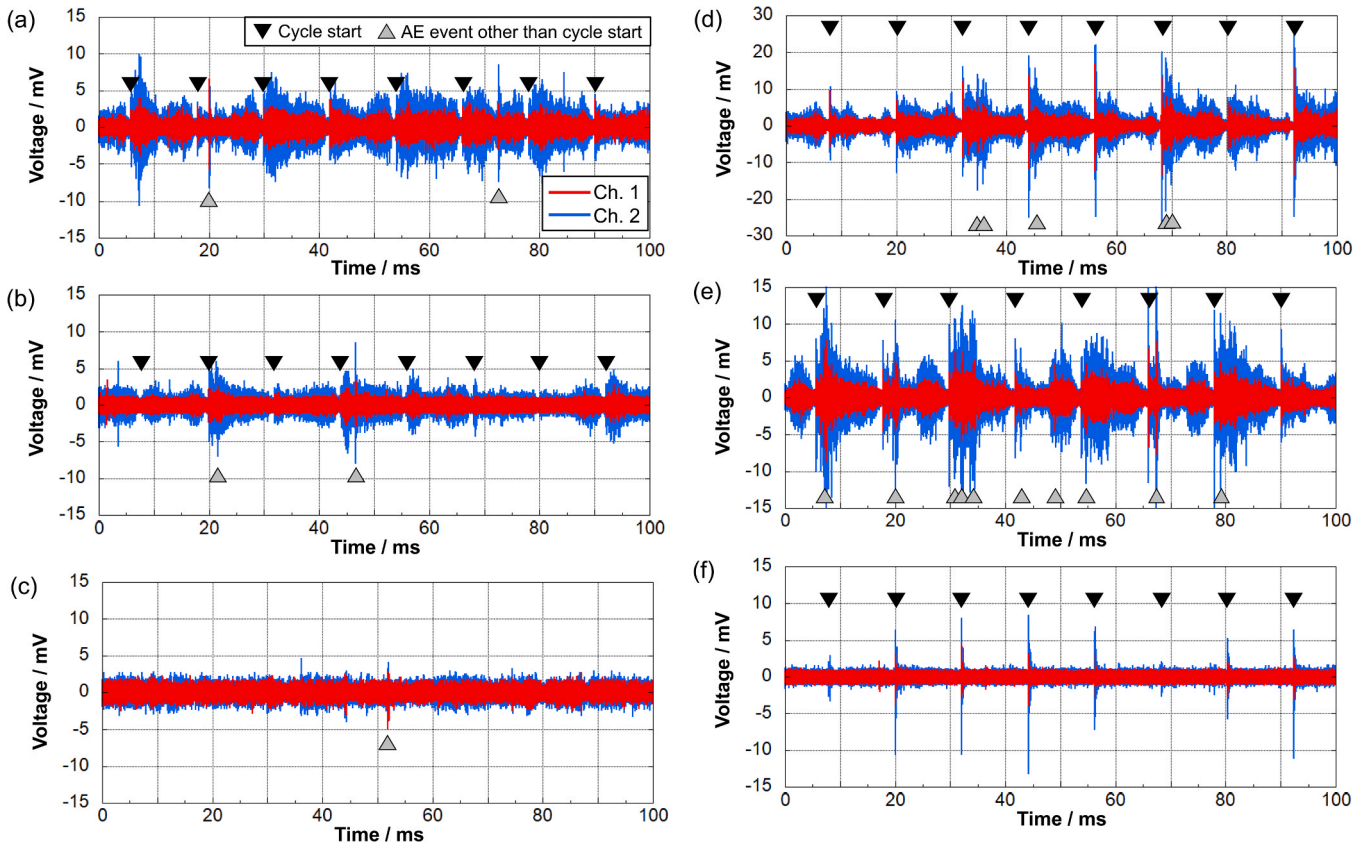

Fig. 6. Sample continuous waveform during multi-track tests (a) M1, (b) M2, (c) M3, (d) M4, (e) M5 and (f) M6.

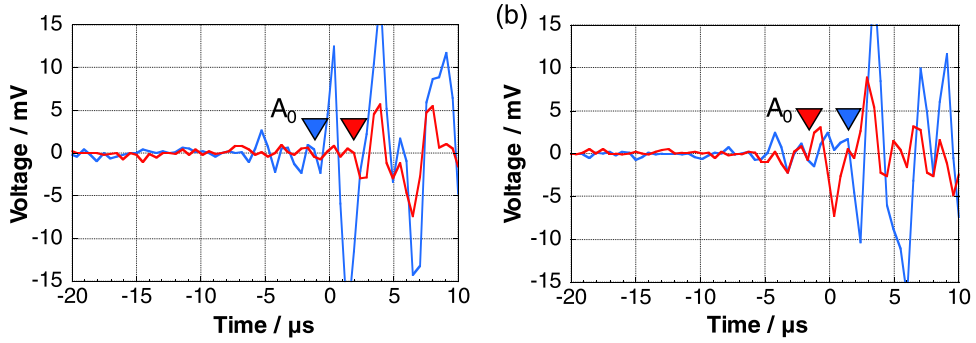

Fig. 7. Burst-type AE event waveform detected at the arrival of a cycle in multi-track test M5: (a) odd-numbered (11th) cycle and (b) even-numbered (12th) cycle.

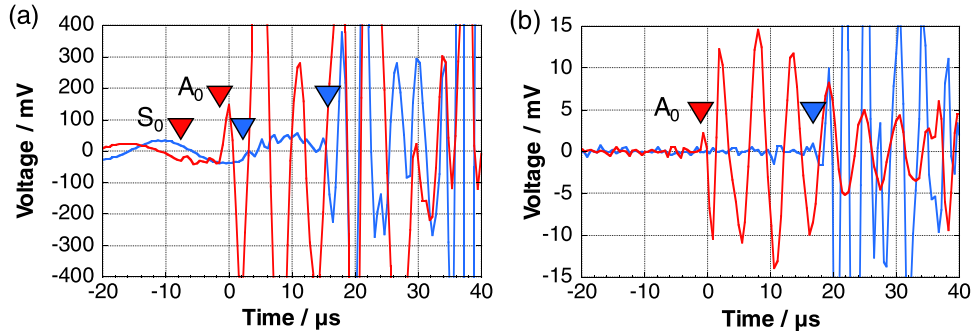

Fig. 8. AE event waveform detected after laser irradiation: (a) after test M2 (position located in the region irradiated in test M1) and (b) after test M4.

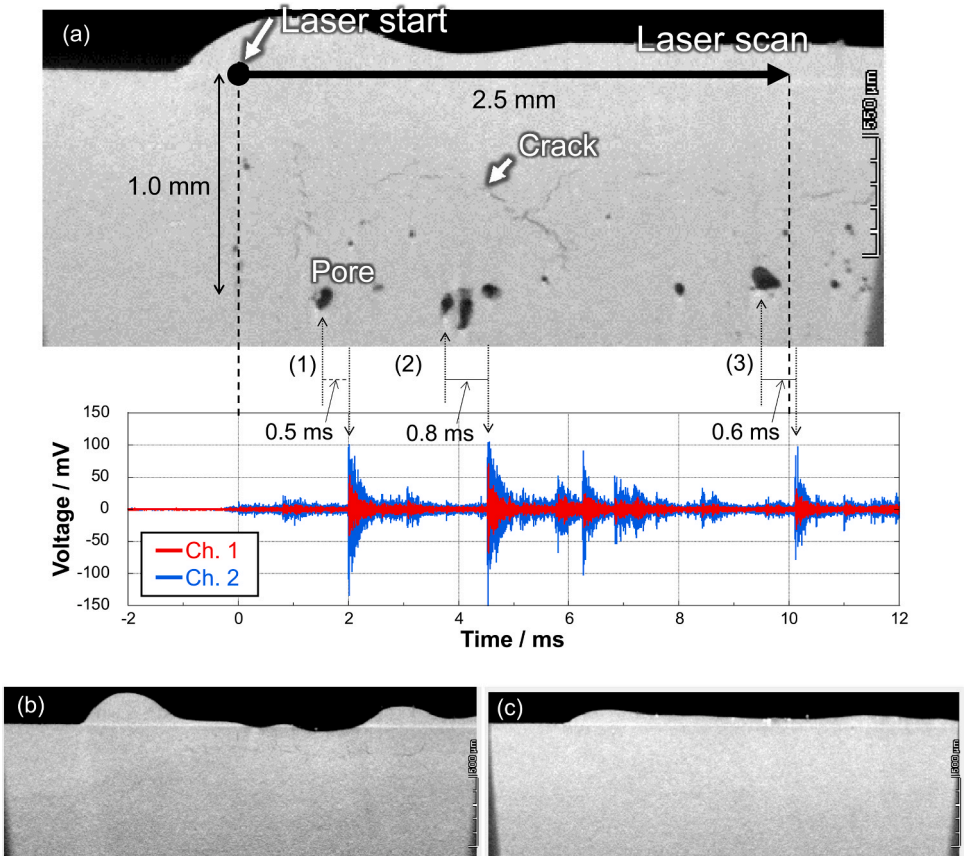

Fig. 9. (a) X-ray CT image after single-track test S4 and AE continuous waveform corresponding to the laser scanning speed, (b) test S5 and (c) test S6.

(180 W and 100 μm hatch distance), a 12.0 ms repeat pattern was observed that originated at the AE event, as shown by downward-pointing black triangles in the figure. The laser scanning speed was 900 mm/s, thus the time necessary to scan 10 mm long track was 11.1 ms. In reality, as discussed below for the M4 test, there was a pause of 0.9 ms between completion of the irradiation of one track and irradiation of the next track in the opposite direction. The 12.0 ms cycle therefore corresponded to one track.

AE events occurred at the onset of each 12.0 ms cycle, but there was a difference in the waveform arrival time between odd- and even-numbered cycles. For example, Fig. 7 shows the waveform near the rising edge for cycles 11 and 12 in test M5, which was conducted almost equidistant from the two sensors. These were small amplitude events, so only the rising edge of the A_0 mode was clearly identifiable. Sensor ch. 2 was earlier by 3.1 μs in cycle 11 and ch. 1 was earlier by 3.1 μs in cycle 12. Converting the time differences into positions by using Fig. 2(b) revealed that the positions where the AE events occurred and the positions of laser irradiation agreed well, as was the case in the single-track tests. In most multi-track tests, AE events were not detected after laser irradiation as in the single-track tests. However, the event shown in Fig. 8(a) was detected 0.4 s after irradiation in test M2 (360 W and 100 μm hatch distance). The amplitude of this event was very large, so that the waveform rising edge of both S_0 and A_0 modes were identifiable. In ch. 1, detection was earlier by 10.2 and 17.4 μs for the S_0 and A_0 modes, respectively. Fig. 2(a) and (b) suggest that this time difference is in the region for test M1, which was conducted before test M2. Furthermore, in test M4 (540 W and 25 μm hatch distance) with the largest input energy density, 12 events were detected between 0.2 and 3.0 s after the end of irradiation, and an additional event was detected 67.0 s after irradiation. Since the waveforms of these events were very similar, only one representative example is shown in Fig. 8(b). Only the waveform rising edge of the A_0 mode could be confirmed because the amplitude of this event was small, and ch. 1 was 18.9 μs earlier. This time difference is in the region of test M4 according to Fig. 2(a) and (b). All other events detected after test M4 were similarly located in the region of test M4.

4. Discussion

In single-track tests, all AE events which could be located near the laser spot is shown in Fig. 5. Therefore, it can be said that AE occurred simultaneously with the large temperature change in which the powder and substrate melted and solidified by the laser irradiation. Estimation of the cause of the AE event requires precise information regarding the relative positions of the laser irradiation and the AE event to confirm when the event occurred during the melting and solidification process. However, as mentioned earlier, the resolution of source location in the tests was 0.74 mm, and the actual error could be several times larger. Therefore, a higher precision in AE source location than that determined from Fig. 5 cannot be expected. Then, the specimen after testing was examined by X-ray CT, and the cross-section at the track line and the AE continuous waveform were compared. Fig. 9(a) shows the region near the start of the track in test S4 (700 W and 250 mm/s). Here, the time axis (horizontal axis) of the waveform matches the scale of the X-ray CT

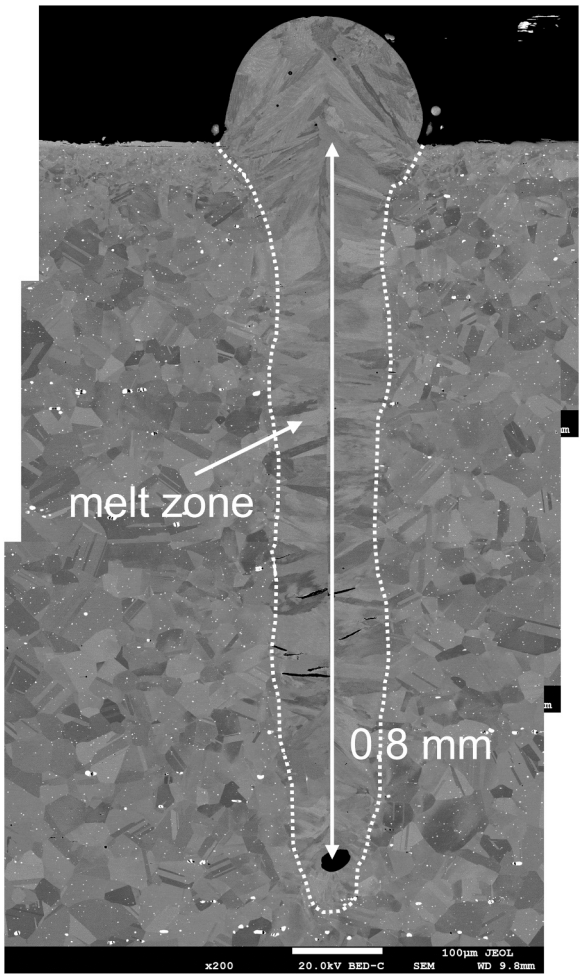

Fig. 10. SEM cross-section image of a sample irradiated with 500 W and 250 mm/s condition.

image and the laser scanning speed (250 mm/s). In other words, 10 ms of the waveform and 2.5 mm of the X-ray CT image are shown with the same length in Fig. 9(a). The track cross-section contained pores, considered to form at the tip of the melt pool, lined up at a depth of approximately 1.0 mm from the substrate surface. In addition, many cracks were found that were likely to have formed at the center of the melt zone (depth 0.5–1.0 mm). The very high energy density that was applied might have produced deep melt pools that caused the formation of the keyhole-shaped and solidification cracks.

The starting point of laser irradiation was estimated to be the filled circle in Fig. 9(a) based on traces in the CT image; this point was therefore corresponded to the irradiation start time in the waveform (0 ms). Then, in the large pores (1)-(3), it can be seen that a large amplitude AE events were found 0.4–0.8 ms after the laser passed directly above. These pores are known to form near the deepest part of the melt zone when the laser power is high. Fig. 10 shows an example of scanning electron microscopy image of a cross-section of the specimen subjected to laser irradiation with 500 W and 250 mm/s condition, which is slightly weaker than test S4. The accurate shape of the melt zone which is surrounded by the dotted line is evident from the shape of the crystal grain, and the pore is near the deepest point. The deepest point should only be in a molten state for a very short time when the laser spot is almost directly above. Therefore, AE events that were detected with a one-to-one correspondence with pores with a delay of about 0.5 ms after the laser spot passed directly above, as in Fig. 9(a), are believed to correspond to the formation of a pore. On the other hand, the waveform in Fig. 9(a) contains many AE events that do not correspond to pore positions, which are considered to arise from generation and propagation of cracks based on correspondence with the X-ray CT image. As shown in Fig. 5, all located AE events were detected within about 20 ms after the laser passed directly above their position; AE events that did not correspond to the pores occurred at the time that the laser passed over and therefore happened as a result of the generation and propagation of a solidification crack. Microcracks might produce AE events during propagation after their generation; consequently, it is normal that one crack corresponds to multiple events. On the other hand, Fig. 9(b) and (c) are X-ray CT images near the start of the track in test S5 and S6, respectively. No vacancies were found in these images. Only a few cracks were seen in Fig. 9(b), but they were not detected in Fig. 9(c). This can be corresponded to the fact that almost no AE events were detected in these tests, as shown in Fig. 3(b) and (c).

By understanding the behavior in single-track tests, as discussed above, it is possible to explain why AE events were often detected when the laser spot turns in multi-track tests. At the turning point, the laser was immediately turned off, moved to the next track position, turned on, and then accelerated to the set value. As a consequence, the local input energy became high and, as in the test S4 shown in Fig. 9, a pore formed in a deep position in the specimen might have led to the occurrence of AE. Fig. 11 shows an X-ray CT image of a section near a turning point in test M1 (540 W, 900 mm/s, and 100 μm hatch distance). Almost all pores in the specimen were found at turning points, and these pores occurred on a line at 0.2 mm intervals, which is twice the hatch distance. This corresponds to the fact that irradiation was conducted in a zigzag pattern. A schematic diagram of this pore formation is shown in Fig. 12. The end point of the previous track became hot due to laser irradiation. After the 0.9 ms interval, the next track starts 0.1 mm away from this hottest point. Therefore, the heat input at this track start point was locally higher than the others, and a pore was generated similar to that in the cases of the test S4 (Fig. 9). As shown in Fig. 3(b), there were barely any AEs corresponding to pore formation in single track tests without turning points, even in test S5 (700 W and 900 mm/s) with a larger laser power than all multi-track tests.

Based on the consideration so far, the timing of AE events during the multi-track tests is summarized in Fig. 13. As previously described, there was a difference between the odd- and even-numbered tracks, so the timing in one round trip (about 24 ms) was shown in this figure. The origin (0 ms) of the timing is the start of the odd-numbered track. Therefore, AE events lined up at 0 ms and 12 ms are corresponded to the pore formation at the start of an odd- and an even-numbered tracks, respectively. Especially, it is a remarkable result that almost all AE events were this type in test M6. On the other hand, many AE events were detected other than the track start in tests M1, M2, M4 and M5. Considering from the results of the single track test (Fig. 9), these AE events can be said to correspond to the transverse cracks which were found in the CT image (Fig. 11). Since many AE events and cracks were detected, it is difficult to make a one-to-one correspondence, but it can be said that it is effective to estimate the crack concentration part from the AE event distribution.

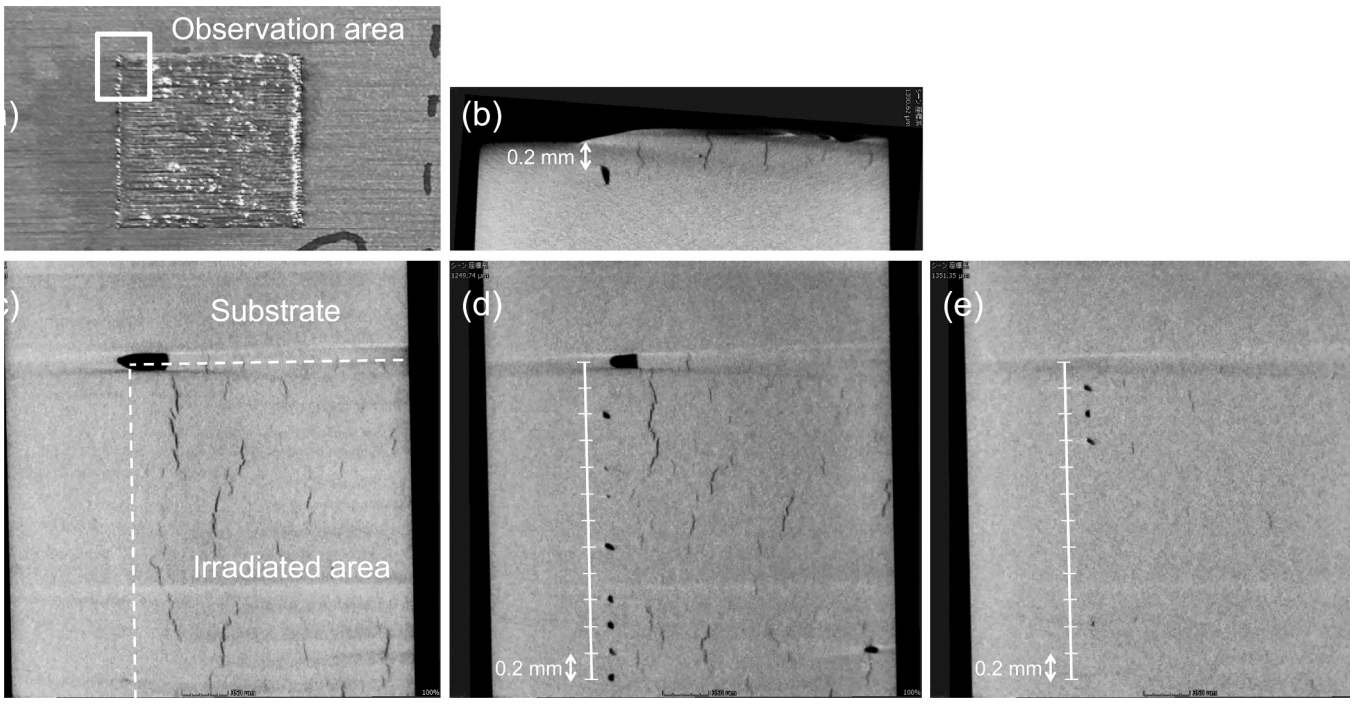

Fig. 11. X-ray CT image near the track turning point in test M1 (540 W, 900 mm/s and 100 μm hatch distance), (a) observation area in the entire irradiated area, (b) cross section image, (c) depth 0.1 mm, (b) 0.2 mm and (c) 0.3 mm from the sample surface.

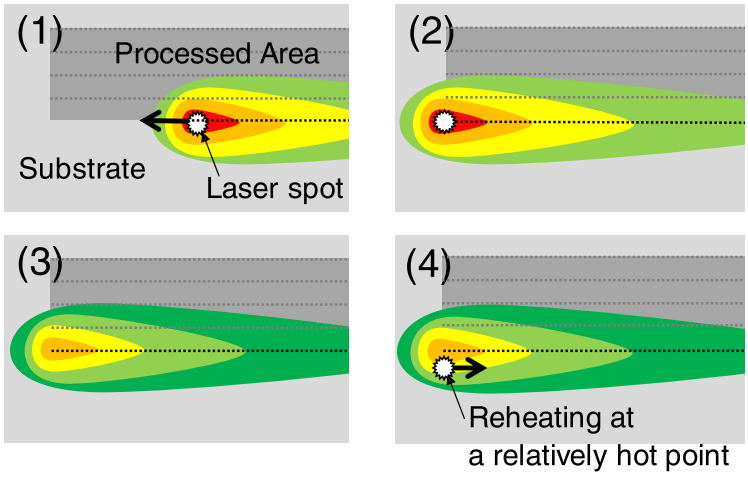

Fig. 12. Schematic diagram of thermal history around the track turning point, (1) irradiating the previous track, (2) end of the previous track, (3) cooling / preparing the next track (0.9 ms) and (4) start of the next track.

5. Conclusions

Pores and microcrack generation during the SLM process was monitored in real time by a convenient method using battery-powered proprietary equipment capable of continuous AE waveform measurement in conjunction with wireless data transmission. This monitoring method does not require modification of the SLM processing equipment. To clarify the detection capabilities of this method and to estimate the causes of microcrack generation, monitoring was conducted in single-track and multi-track tests of a single-layer instead of an additive manufacturing (multi-layer) test system, and the results were compared with sample cross-section observations after the tests. Many burst type AE events were detected during processing. Pores and microcracks formed under high-laser-intensity conditions, and AE events corresponding to these pores and microcracks were detected. In multi-track tests, crack generation slightly after laser irradiation and from zig-zag irradiation was detected, and the positions of AE events were located with an error of few millimeters. These results demonstrate the high capabilities of this method to detect and locate microcrack formation in additive manufacturing. In summary, if the laser irradiation position and the AE source location are close to each other, the AE is considered to have occurred at the laser irradiation position. It enables very accurate positioning. On the other hand, if the laser irradiation position and the AE source location are far apart, then the AE location should be used. It includes an error of 2–3 mm, but enables the correct localization of delayed events. This method should be directly applicable to a normal, multi-layer process and is therefore very effective for monitoring SLM processes.

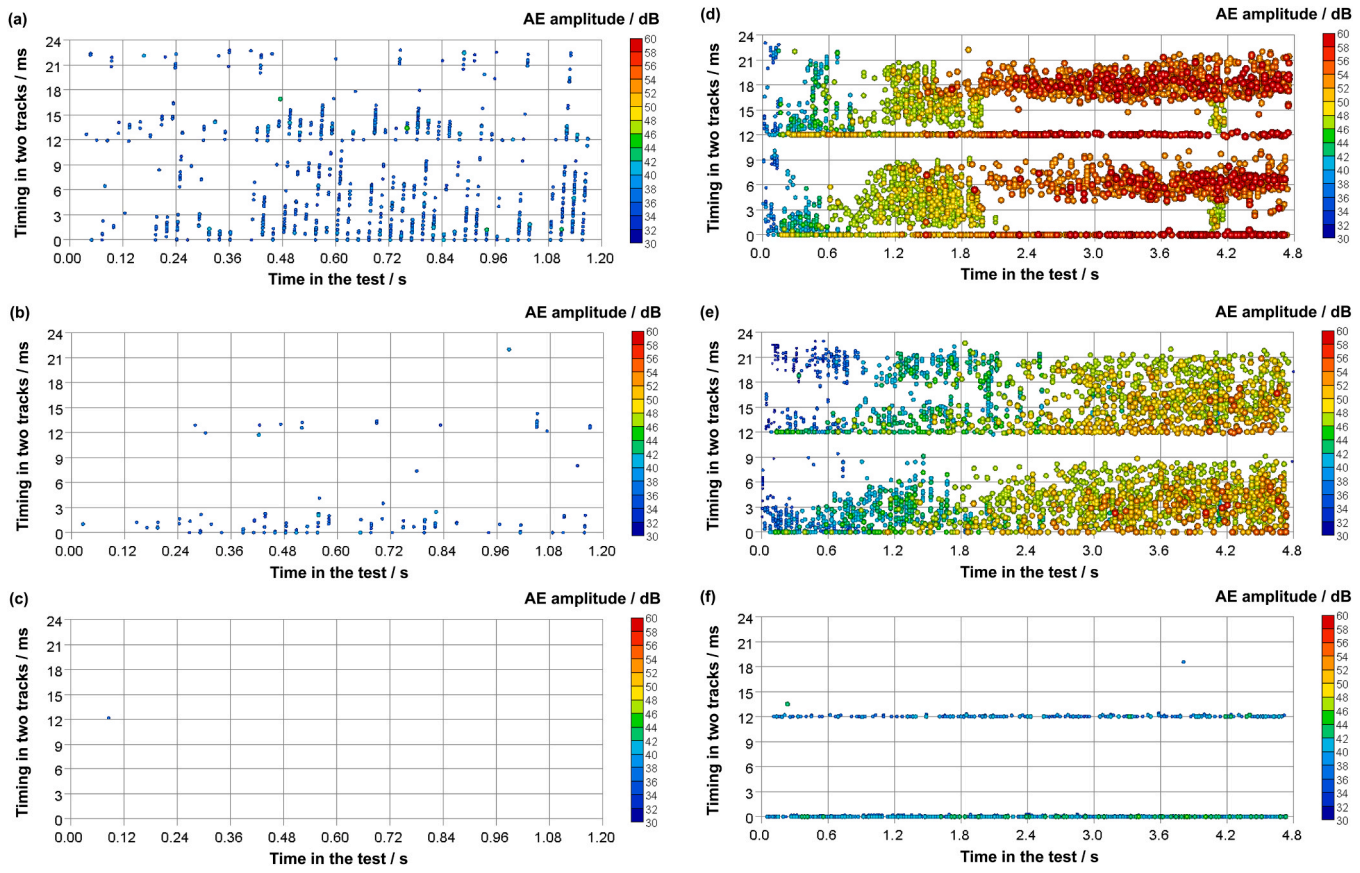

Fig. 13. AE timing in each two tracks during multi-track tests (a) M1, (b) M2, (c) M3, (d) M4, (e) M5 and (f) M6.

Declaration of Competing Interest

The authors declare that they have no known competing financial interests or personal relationships that could have appeared to influence the work reported in this paper.

Acknowledgements

This work was supported by Council for Science, Technology and Innovation (CSTI), Cross-ministerial Strategic Innovation Promotion Program (SIP), "Materials Integration for revolutionary design system of structural materials" (Funding agency: Japan Science and Technology Agency (JST)).

References

[1] N.J. Harrison, I. Todd, K. Mumtaz, Reduction of micro-cracking in nickel superalloys processed by selective laser melting: a fundamental alloy design approach, Acta Mater. 94 (2015) 59–68, https://doi.org/10.1016/j.actamat.2015.04.035.

[2] G. Marchese, G. Basile, E. Bassini, A. Aversa, M. Lombardi, D. Ugues, P. Fino, S. Biamino, Study of the microstructure and cracking mechanisms of Hastelloy X produced by laser powder bed fusion, Materials 11 (2018) 106–117, https://doi.org/10.3390/ma11010106.

[3] S.A. Shevchik, C. Kenel, C. Leinenbach, K. Wasmer, Acoustic emission for in situ quality monitoring in additive manufacturing using spectral convolutional neural networks, Addit. Manuf. 21 (2018) 598–604, https://doi.org/10.1016/j.addma.2017.11.012.

[4] S.A. Shevchik, G. Masinelli, C. Kenel, C. Leinenbach, K. Wasmer, Deep learning for in situ and real-time quality monitoring in additive manufacturing using acoustic emission, IEEE Trans. Ind. Inform. 15 (2019) 5194–5203, https://doi.org/10.1109/TII.2019.2910524.

[5] S.A. Shevchik, T. Le-Quang, B. Meylan, F.V. Farahani, M.P. Olbinado, A. Rack, G. Masinelli, C. Leinenbach, K. Wasmer, Supervised deep learning for real-time quality monitoring of laser welding with X-ray radiographic guidance, Sci. Rep. 10 (2020) 3389, https://doi.org/10.1038/s41598-020-60294-x.

[6] N. Eschner, L. Weiser, B. Häfner, G. Lanza, Classification of specimen density in Laser Powder Bed Fusion (L-PBF) using in-process structure-borne acoustic process emissions, Addit. Manuf. 34 (2020), 101324, https://doi.org/10.1016/j.addma.2020.101324.

[7] F. Wang, H. Mao, D. Zhang, X. Zhao, Y. Shen, Online study of cracks during laser cladding process based on acoustic emission technique and finite element analysis, Appl. Surf. Sci. 255 (2008) 3267–3275, https://doi.org/10.1016/j.apsusc.2008.09.039.

[8] D. Kouprianoff, N. Luwes, E. Newby, L. Yadroitsava, I. Yadroitsev, On-line monitoring of laser powder bed fusion by acoustic emission: Acoustic emission for inspection of single tracks under different powder layer thickness, 2017 Pattern recognition association of South Africa and robotics and mechatronics international conference (PRASA-RobMech), 203–207.

[9] C. Prieto, R. Fernandez, C. Gonzalez, M. Diez, J. Arias, R. Sommerhuber, F. Lucking, In situ process monitoring by optical microphone for crack detection in Laser Metal Deposition applications, 11th CIRP Conference on Photonic Technologies (LANE 2020).

[10] C.H. Palmer, R.E. Green Jr., Materials evaluation by optical detection of acoustic emission signals, Mater. Eval. 35 (1977) 107–112.

[11] C.H. Palmer, R.E. Green Jr., Optical detection of acoustic emission waves, Appl. Opt. 16 (1977) 2333–2334.

[12] M. Enoki, M. Watanabe, P. Chivavibul, T. Kishi, Non-contact measurement of acoustic emission in materials by laser interferometry, Sci. Tech. Adv. Mater. 1 (2000) 157–165, https://doi.org/10.1016/S1468-6996(00)00017-6.

[13] M. Watanabe, M. Enoki, T. Kishi, Fracture behavior of ceramic coatings during thermal cycling evaluated by acoustic emission method using laser interferometers, Mater. Sci. Eng. A 359 (2003) 368–374, https://doi.org/10.1016/S0921-5093(03)00394-0.

[14] K. Ito, H. Kuriki, M. Watanabe, S. Kuroda, M. Enoki, Detection of AE events due to cracks in TBC during spraying process, Mater. Trans. 53 (2012) 671–675, https://doi.org/10.2320/matertrans.MBW201118.

[15] K. Ito, H. Kuriki, H. Araki, S. Kuroda, M. Enoki, Detection of segmentation cracks in top coat of thermal barrier coatings during plasma spraying by non-contact acoustic emission method, Sci. Technol. Adv. Mater. 15 (2016), 035007, https://doi.org/10.1088/1468-6996/15/3/035007.

[16] Á. Lédeczi, T. Hay, P. Volgyesi, D.R. Hay, A. Nádas, S. Jayaraman, Wireless acoustic emission sensor network for structural monitoring, IEEE Sens. J. 9 (2009) 1370–1377, https://doi.org/10.1109/JSEN.2009.2019315.

[17] K. Ito, K. Takahashi, M. Enoki, Noise tolerant and wireless AE measurement system for process monitoring, J. Acoust. Emiss. 36 (2019) S23–S26.

[18] K. Ito, M. Enoki, Acquisition and analysis of continuous acoustic emission waveform for classification of damage sources in ceramic fiber mat, Mater. Trans. 48 (2007) 1221–1226, https://doi.org/10.2320/matertrans.I-MRA2007850.
[19] D.L. Donoho, De-noising by soft-thresholding, IEEE Trans. Inf. Theory 41 (1995) 613–627, https://doi.org/10.1109/18.382009.
[20] N.N. Hsu, F.R. Breckenridge, Characterization and calibration of acoustic emission sensors, Mater. Eval. 39 (1981) 60–68.
[21] H. Akaike, A new look at the statistical model identification, IEEE Trans. Autom. Control 19 (1974) 716–723.
[22] P. Sedlak, Y. Hirose, S.A. Khan, M. Enoki, J. Sikula, New automatic localization technique of acoustic emission signals in thin metal plates, Ultrasonics 49 (2009) 254–262, https://doi.org/10.1016/j.ultras.2008.09.005.
[23] K. Ito, M. Enoki, High-precision source location of AE event using automatic error correction of signal rising time, J. Acoust. Emiss. 34 (2017) S46–S49.